

AD-A168 217

THE PREDICTION OF TRANSONIC LOADING ADVANCING
HELICOPTER ROTORS(U) NATIONAL AERONAUTICS AND SPACE
ADMINISTRATION HOFFETT FIELD C. R STRAWN ET AL.
APR 86 NASA-A-86198 NASA-TN-88238

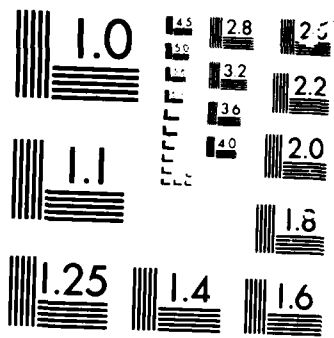
1/1

UNCLASSIFIED

F/G 1/3

NL





M-1000

1000

AD-A168 217

DTIC
ELECTE
MAY 12 1986
S D

The Prediction of Transonic Loading on Advancing Helicopter Rotors

Roger Strawn and C. Tung

April 1986

DTIC FILE COPY

DISTRIBUTION STATEMENT A
Approved for public release;
Distribution Unlimited

NASA
National Aeronautics and
Space Administration

United States Army
Aviation Systems
Command



100

The Prediction of Transonic Loading on Advancing Helicopter Rotors

Roger Strawn and C. Tung, Aeroflightdynamics Directorate, U. S. Army Aviation and Technology Activity, Ames Research Center, Moffett Field, California

April 1986

NASA

National Aeronautics and
Space Administration

Ames Research Center
Moffett Field, California 94035

United States Army
Aviation Systems
Command
St. Louis, Missouri 63120



THE PREDICTION OF TRANSONIC LOADING ON ADVANCING HELICOPTER ROTORS

R. C. Strawn and C. Tung

U.S. Army Aeroflightdynamics Directorate, AVSCOM
NASA Ames Research Center
Moffett Field, California 94035 USA

SUMMARY

Two different schemes are presented for including the effect of rotor wakes on the finite-difference prediction of rotor loads. The first formulation includes wake effects by means of a blade-surface inflow specification. This approach is sufficiently simple to permit coupling of a full-potential finite-difference rotor code to a comprehensive integral model for the rotor wake and blade motion. The coupling involves a transfer of appropriate loads and inflow data between the two computer codes. Results are compared with experimental data for two advancing rotor cases. The second rotor-wake modeling scheme in this paper is a "split potential" formulation for computing unsteady blade-vortex interactions. Discrete vortex fields are introduced into a three-dimensional, conservative, full-potential rotor code. Computer predictions are compared with two experimental blade-vortex interaction cases.

LIST OF SYMBOLS

- a_{∞} = freestream speed of sound
- AR = aspect ratio, R/c
- c = rotor chord length
- C_l = lift coefficient
- C_p = pressure coefficient
- C_T = rotor thrust coefficient
- G = prescribed velocity potential
- h = nondimensional time step
- I = identity matrix
- J = Jacobian of coordinate transform matrix
- M_T = hover tip Mach number
- n = superscript representing current time level
- r = distance along the rotor in the spanwise direction
- \hat{r} = radial coordinate in Fig. (1)
- R = radial distance to the rotor tip
- R_{∞} = free stream subtraction term in Eq. (5)
- t = normalized time in the untransformed coordinate system
- U = contravariant velocity normal to the η, ζ plane
- V = contravariant velocity normal to the ξ, ζ plane
- W = contravariant velocity normal to the ξ, η plane
- x, y, z = untransformed coordinate system
- X = chordwise distance along the rotor
- y = spanwise coordinate in Fig. (1)
- Z_c = vortex core distance to the airfoil centerline
- α = angle of attack, deg.
- $\tilde{\beta}$ = $\rho^2 \gamma / J$
- Γ = jump in potential across the wake normalized by $(a_{\infty} c)$
- Γ_v = vortex strength normalized by $(a_{\infty} c)$
- γ = specific heat ratio
- μ = rotor advance ratio
- Φ = total velocity potential
- ϕ = perturbation velocity potential
- ψ = rotor azimuthal angle, deg.

Accession For	
NTIS CRA&I	<input checked="" type="checkbox"/>
DTIC TAB	<input type="checkbox"/>
Unannounced	<input type="checkbox"/>
Justification	
By	
Distribution /	
Availability Codes	
Dist	Avail and/or Special
A-1	

ρ	fluid density normalized by free-stream values
σ	rotor solidity
τ	normalized time in the transformed coordinate system
$\hat{\rho}$	ρ/J
θ	coordinate angle in Fig. (1)
ξ, η, ζ	transformed coordinate system

1. INTRODUCTION

Accurate methods for flow prediction on helicopter rotors are an important part of the rotor design process. Integral methods with prescribed wakes are routinely used for these flow-field predictions. An example of this type of approach is found in Ref. 1. However, integral techniques, such as panel and lifting-surface methods, are unable to treat transonic flow nonlinearities. This problem is a fundamental limitation of this methodology.

Alternatives to integral methods are finite-difference schemes that compute three-dimensional transonic flows around rotor blades. These methods typically solve the Euler equations, full-potential equations, or the small disturbance potential equations. These finite-difference methods have the advantage over other methods because they are designed to compute the transonic flow nonlinearities that are associated with high-speed advancing rotors. The disadvantage of these methods is that computer speed and storage requirements limit the size of the computational domain. The complexities of the rotor wake system usually extend well outside of typical finite-difference grids for helicopter rotors.

To surmount these problems, several hybrid approaches have been developed that couple integral methods for the rotor wakes to finite-difference methods for the transonic flow over the rotor blades. Examples of these methods are given in Refs. 2 through 7. These approaches have been quite successful in predicting the aerodynamic loading on realistic helicopter rotors.

Reference 7 presents an unsteady, three-dimensional, finite-difference method for computing the flow-field over advancing helicopter rotors. This method solves the full-potential equations in strong conservation form. This paper also demonstrated a hybrid approach for including a rotor wake system into a hover computation. Vortex elements located close to the blade were modeled as discrete vortices inside the finite-difference computation. Vortices in the far-field were included using an integral wake model.

The present paper has two objectives, both of which build on the results presented in Ref. 7. The first objective is to couple the Full-Potential Rotor code (FPR) in Ref. 7 to the integral wake modeling of the CAMRAD code in Ref. 1. The coupling scheme will be similar to those presented in Refs. 2 through 6. Although the coupling scheme has been used before with other finite-difference codes, the objective is to demonstrate its use with the FPR code.

The second objective in this paper deals with a much more detailed representation of rotor blade-vortex interactions. The idea is to extend the finite-difference vortex modeling in Ref. 7 to compute unsteady problems. A single vortex is placed directly into the computational domain and the blade-vortex interaction is examined in detail. At present, the added complexity of the unsteady vortex limits this analysis to small numbers of vortices and relatively simple geometries.

2. FORMULATION OF THE FULL-POTENTIAL EQUATIONS

The basic FPR code used in this paper is described in Ref. 7. It solves the unsteady full-potential equation in strong conservation form. The rotor code is based on the fixed-wing code of Bridgeman et al. [8].

The full-potential equation is written in a generalized coordinate system as follows:

$$\frac{\partial}{\partial \tau} \left(\frac{\rho}{J} \right) + \frac{\partial}{\partial \xi} \left(\frac{\rho U}{J} \right) + \frac{\partial}{\partial \eta} \left(\frac{\rho V}{J} \right) + \frac{\partial}{\partial \zeta} \left(\frac{\rho W}{J} \right) = 0 \quad (1)$$

with density given by:

$$\rho = \left\{ 1 - \frac{\gamma}{2} \left[2\Phi_r + (U + \xi_t)\Phi_\xi + (V + \eta_t)\Phi_\eta + (W + \zeta_t)\Phi_\zeta \right] \right\}^{1/\gamma} \quad (2)$$

where

$$\begin{aligned} U &= \xi_t + A_1\Phi_\xi + A_4\Phi_\eta + A_5\Phi_\zeta \\ V &= \eta_t + A_4\Phi_\xi + A_2\Phi_\eta + A_6\Phi_\zeta \\ W &= \zeta_t + A_5\Phi_\xi + A_6\Phi_\eta + A_3\Phi_\zeta \end{aligned} \quad (3)$$

and

$$\begin{aligned}
A_1 &= \xi_x^2 + \xi_y^2 + \xi_z^2 \\
A_2 &= \eta_x^2 + \eta_y^2 + \eta_z^2 \\
A_3 &= \zeta_x^2 + \zeta_y^2 + \zeta_z^2 \\
A_4 &= \xi_x \eta_x + \xi_y \eta_y + \xi_z \eta_z \\
A_5 &= \xi_x \zeta_x + \xi_y \zeta_y + \xi_z \zeta_z \\
A_6 &= \eta_x \zeta_x + \eta_y \zeta_y + \eta_z \zeta_z
\end{aligned} \tag{4}$$

All velocities are normalized by a_∞ , distances by the airfoil chord length, and time by the combination (c/a_∞) . Density is normalized by the free-stream value.

Equation (1) is solved by using first-order backward differencing in time and second-order central differencing in space. The temporal density derivative is locally linearized about the old time levels in a manner that preserves the conservative form (see Ref. 8).

The resulting equation is approximately factored into ξ , η , and ζ operators.

$$\begin{aligned}
& \left[I + hU^n \delta_\xi - \frac{h^2}{\beta^n} \delta_\xi (\hat{\rho} A_1)^n \delta_\xi \right] \times \left[I + hV^n \delta_\eta - \frac{h^2}{\beta^n} \delta_\eta (\hat{\rho} A_2)^n \delta_\eta \right] \times \\
& \left[I + hW^n \delta_\zeta - \frac{h^2}{\beta^n} \delta_\zeta (\hat{\rho} A_3)^n \delta_\zeta \right] (\Phi^{n+1} - \Phi^n) = \frac{h^2}{\beta^n} \left[\delta_\xi (\hat{\rho} \bar{U})^n + \delta_\eta (\hat{\rho} \bar{V})^n + \delta_\zeta (\hat{\rho} \bar{W})^n - R_\infty \right] + C
\end{aligned} \tag{5}$$

where δ_ξ , δ_η , and δ_ζ represent central difference operators in space and the term C is given by Eq. (6). The bracketed term in Eq. (6) represents the temporal conservation correction to the algorithm.

$$\begin{aligned}
C &= (\Phi^n - \Phi^{n-1}) + \left[\frac{\hat{\beta}^{n-1}}{\beta^n} (\Phi^n - 2\Phi^{n-1} + \Phi^{n-2}) + \frac{h}{\hat{\beta}^n} (\hat{\rho}^n - \hat{\rho}^{n-1}) \right. \\
& \left. + h \frac{\hat{\beta}^{n-1}}{\beta^n} (U^{n-1} \delta_\xi + V^{n-1} \delta_\eta + W^{n-1} \delta_\zeta) (\Phi^n - \Phi^{n-1}) \right]
\end{aligned} \tag{6}$$

A steady state ADI relaxation algorithm can be obtained from Eq. (5) by omitting the unsteady C term on the right-hand side of the equation.

The streamwise flux terms use upwind density biasing in regions of supercritical flow to ensure stability of the algorithm. Details are given in Ref. 8. The quantity R_∞ represents a numerical truncation error term caused by incomplete metric cancellation. Formulation of this correction term is discussed in Ref. 8.

3. GRID AND BOUNDARY CONDITIONS

Rotor flow fields are computed by modifying the time-metric terms ξ_t , η_t , and ζ_t in Eqs. (2) and (3). The finite-difference grid is attached to the rotor blade which moves through still air. Each grid point has an appropriate rotational and translational coordinate velocity field given by ξ_t , η_t , and ζ_t . This results in free-stream conditions that are given by $\Phi = 0$. A spanwise series of planar parallel O-grids have been chosen for the finite-difference mesh. This results in a very efficient use of grid points. Grid size for a typical rotor case is 80 chordwise points, 19 spanwise points, and 25 points normal to the surface. The radial location of the outer grid boundary typically varies from 7 to 10 chords from the rotor surface.

A surface transpiration condition is implemented on the rotor surface in order to simulate angle of attack conditions. The transpiration condition can be written as $\Phi_n = (\Phi_s + s_t) \tan \alpha$, where α is the desired angle of attack, s_t represents the surface coordinate motion, and the s and n directions are tangential and normal to the airfoil surface respectively. Along the inner boundary plane, normal to the rotor, the spanwise contravariant velocity V , is set equal to η_t .

For lifting cases, the shed vorticity is specified as a jump in potential, Γ , imposed across the coordinate plane $\xi = 0$. This coordinate plane is approximately aligned with the shear layer from the trailing edge. An unsteady transport equation for this potential jump is imposed across the wake. It is derived by assuming that density is continuous across the cut, and can be written as:

$$\Gamma_r + \langle V \rangle \Gamma_n + \langle W \rangle \Gamma_\zeta = 0 \tag{7}$$

where $\langle V \rangle$ and $\langle W \rangle$ are the averages of the contravariant velocities above and below the wake.

At the outer grid boundary, a nonreflection boundary condition has been implemented similar to that used in Ref. 9. If we make the assumption that disturbances propagate only in the radial and spanwise directions at the outer boundary of the O-grid, then a nonreflection boundary condition can be written as:

$$\phi_t + ((M_\infty)_r \cos \theta - 1) \phi_r + (M_\infty)_y \phi_y = 0 \tag{8}$$

where the radial coordinate r and the angle θ are defined in Fig. 1. The values $(M_\infty)_z$ and $(M_\infty)_y$ are the free-stream Mach number components relative to the blade-fixed grid.

Equation (8) is used to explicitly update the solution on the outer boundary. It is applied after each time-step for the interior points. Implementation of Eq. (8) was necessary for unsteady lifting rotor cases so that the accumulation of disturbances at the outer boundary could be prevented.

4. WAKE MODELING FOR FORWARD FLIGHT COMPUTATIONS

Lifting rotors in forward flight have wake systems that are too complicated to model directly in the current finite-difference full-potential scheme. In addition, there is no easy way to couple the blade trim solution directly into a finite-difference model. A way to circumvent these difficulties is to couple the FPR code for the rotor aerodynamic loads to the CAMRAD integral method [1] for modeling the rotor wake and blade motion. The basic coupling scheme is the same as that described in Refs. 4 and 5.

The CAMRAD code is a fast and efficient model for comprehensive rotor performance analysis. It normally models the aerodynamic loads through equivalent angles of attack for the rotor that result from the trimmed-rotor and wake system. It then uses table lookups of two-dimensional airfoil data to determine the blade lift coefficients. These table lookups do not model the flow-field unsteadiness or three-dimensionality that is present in actual advancing rotor cases. The coupling scheme used in this paper replaces these table lookups with lift coefficients that are determined from finite-difference calculations for the specified partial angles of attack.

The matching of the CAMRAD and FPR codes is summarized in Fig. 2. The process begins by obtaining a trimmed solution from the CAMRAD code with the lift totally obtained from airfoil tables. The CAMRAD solution specifies equivalent angles of attack along the rotor. This rotor twist distribution is used to model the wake effects in the subsequent FPR finite-difference calculation. Unsteady lift values resulting from the FPR calculation are then applied to the next CAMRAD trim solution using the following algorithm.

$$C_l(\alpha) = C_{l_{FPR}}(\alpha_{old}) + C_{l_{airfoil}}(\alpha) - C_{l_{airfoil}}(\alpha_{old}) \quad (9)$$

The blade twist angles α and α_{old} are the angles of attack from the current and previous trim loops, respectively. The particular form of Eq. (9) is chosen to enable the CAMRAD computer program to dynamically update the lift coefficient solution during the calculation. The solution is converged when $\alpha = \alpha_{old}$ and the finite-difference lift is fully consistent with the rotor inflow and motion. Convergence of the scheme is rapid and typically occurs in less than three iterative cycles around the loop in Fig. 2.

5. RESULTS FOR ADVANCING ROTORS

The CAMRAD and FPR code coupling was tested in two cases. The first case is a 1/7-scale model Cobra operational load survey (OLS) rotor that is described in Ref. 10. This stiff-bladed AH-1G model was pressure-instrumented. Data is currently available only on the upper surface of the rotor at $r/R = 0.95$. Tip Mach number, M_T , is 0.663, and advance ratio, μ , is 0.298. The finite-difference computation used 720 equal time-steps in advancing from 0° to 180° . Total computer time for each global iteration of the FPR code was approximately 10 CPU minutes on a CRAY XMP-12 computer.

Figure 3 shows the CAMRAD/FPR pressure predictions for this case at a series of rotor azimuthal angles. Experimental data on the upper blade surface are also shown. Predicted results in the first quadrant show good agreement with the experimental results. At $\psi = 90^\circ$, the prediction shows more expansion at the leading edge than is present in the data although the shock location is predicted quite well.

The negative surface pressures are overpredicted in the second quadrant when they are compared to the data. This is consistent with the results of Tung and Chang [4], who solved a nonconservative form of the full-potential equation coupled to the CAMRAD wake model. It is difficult to determine the exact cause of the discrepancy in the second quadrant. This is particularly curious in light of the fact that the wake structure in the first quadrant is more complex than that in the second quadrant.

The second computed test case was a three-bladed rotor tested at ONERA by Philippe and Chattot [11]. The blade was pressure-instrumented at three radial locations, $r/R = 0.85, 0.90$, and 0.95 . Both upper- and lower-surface pressures were reported in the experiment. Blade tip Mach number M_T is 0.629, and the advance ratio is relatively high at $\mu = 0.387$. Once again, 720 equal time-steps were used from $\psi = 0^\circ$ to $\psi = 180^\circ$.

Figures 4, 5 and 6 show the comparison between prediction and experiment at $r/R = 0.85, 0.90$ and 0.95 respectively. At each radial location, pressure results on the rotor are presented for a series of azimuthal angles. Agreement between the prediction and the data is good, particularly for the upper surface shock location, and for the lower surface expansion near the leading edge. Predicted pressures on the lower surface are slightly higher than those shown by the experimental data, particularly in the second quadrant. However, predicted pressures on the upper surface, are in good agreement with the data. Overall, the evolution of the pressures is well predicted by the combined CAMRAD/FPR method.

6. UNSTEADY BLADE-VORTEX INTERACTION MODEL

Reference 7 describes a method by which discrete vortices could be introduced into the finite-difference computation. The approach is to consider the difference equation (5) in functional form as shown below.

$$\begin{aligned} L(\rho^n, \phi^n, \phi^{n+1} - \phi^n) - R(\rho^n, \phi^n) + C(\rho^n, \rho^{n-1}, \phi^n, \phi^{n-1}, \phi^{n-2}) \\ \rho^n - F(\phi^n) \end{aligned} \quad (10)$$

The first relation represents mass conservation and the second relation is the Bernoulli equation. Note that the L operator in Eq. (10) is linear with respect to $\phi^{n+1} - \phi^n$. This is a result of the original density linearization.

The total potential Φ is now rewritten as the sum of two parts. The first is a known potential, G , which is due to a specified system of vortex elements. The second component is an unknown potential, ϕ , which is the perturbation of G that is due to the rotor and its immediate shed vorticity. If we now substitute the equality, $\Phi = G + \phi$, into Eq. (10), the following form results:

$$\begin{aligned} L(\rho^n, \phi^n, \phi^{n+1} - \phi^n) - R(\rho^n, \phi^n + G^n) + C \begin{pmatrix} \rho^n, \rho^{n-1} \\ \phi^n \\ \phi^{n-1} \\ \phi^{n-2} \end{pmatrix} + C \begin{pmatrix} \rho^n, \rho^{n-1} \\ G^n \\ G^{n-1} \\ G^{n-2} \end{pmatrix} \cdot L(\rho^n, \phi^n, G^{n+1} - G^n) \\ \rho^n - F(\phi^n + G^n) \end{aligned} \quad (11)$$

The left-hand side of Eq. (11) is identical to the original algorithm. The right-hand side and the Bernoulli relation undergo only minor modifications.

For the steady hover problem considered in Ref. 7, the right-hand functions in Eq. (11) contains only spatial gradient terms in G . They can be added to the original FPR code with relatively little effort. An unsteady, forward-flight computation requires that the temporal gradient terms involving G must also be added. Because of the added complexity in programming, some of the temporal gradient terms involving G have not been included at present. The unsteady vortex terms that have been dropped from the right-hand side of the final solution scheme are

$$C \begin{pmatrix} \rho^n, \rho^{n-1} \\ G^n \\ G^{n-1} \\ G^{n-2} \end{pmatrix} \cdot L(\rho^n, \phi^n, G^{n+1} - G^n) \quad (12)$$

However, all spatial and temporal gradient terms resulting from the vortex field have been included in the density and contravariant velocity evaluations.

If the center of a vortex is located far from the rotor surface, say greater than one chord length, then it can be shown analytically that the neglected terms in Eq. (12) are small. For vortex passage distances that are less than one chord, it becomes more difficult to justify this assumption. In this paper, typical vortex passage distances are approximately half a chord length.

Jones [12] has studied the unsteady airfoil-vortex interaction problem for two-dimensional cases. He has modeled an unsteady vortex in a number of different ways. Vortex strengths and passage distances are similar to the three-dimensional cases considered in the present paper. Jones' results show that pressure and lift results from a "branch-cut" vortex model do not differ appreciably from those of a "split-potential" method which neglects the terms in Eq. (12). In the branch-cut model, the vortex is included in the flow as a discontinuity in total potential. The branch-cut method implicitly includes all of the temporal gradient terms that are caused by the vortex, but in a way that is restricted to an H-mesh. References 3 and 12 give a further description of the branch-cut vortex model.

Sankar and Malone [13] also present a series of two-dimensional, blade-vortex calculations. Their model uses a split-potential formulation similar to the one described above. They neglect, however, all of the temporal and many of the spatial derivative terms that result from the vortex field. Vortex strengths and passage distances are similar to the cases considered in this paper. Their airfoil lift results compare favorably with the two-dimensional transonic small-disturbance results of McCroskey [14], the Euler code results of Sankar and Tang [15], and the full-potential results of Jones [12].

The evidence presented above, coupled with our own comparisons to both experimental data and other computer codes, indicates that the neglected terms in Eq. (12) are of little consequence for the vortex strengths and passage distances considered in the present paper. In future work we plan to add the neglected terms to the FPR code to verify this assumption.

Strictly speaking, the vortex velocity field in these calculations must be irrotational since it is derived from the gradient of the potential G . In practice however, we include a small rotational core in our vortex velocity fields in order to prevent the velocities from becoming infinite at the vortex centers.

7. RESULTS FROM UNSTEADY BLADE-VORTEX INTERACTION CASES

To test the vortex model described above, the FPR code was set up to compute the unsteady blade-vortex interaction experiment of Caradonna et al. [16]. In this experiment, a two-bladed NACA 0012 model rotor was tested in a wind tunnel. A NACA 0015 wing was located upstream in the tunnel. It was used to produce a streamwise line-vortex that passed beneath the helicopter rotor. Figure 7 is taken from Ref. 17 and illustrates the experimental design. Pressure data was measured at a single spanwise location on the blade ($r/R = 0.893$). Blade aspect ratio was equal to 7. Srinivasan et al. [17] have previously presented computational results for this experiment using two-dimensional thin-layer Navier Stokes and transonic small-disturbance models.

The first test case is entirely subcritical, with a tip Mach number of 0.6, and an advance ratio of 0.2. At the 0° and 180° azimuthal rotor angles, the line-vortex is located directly under the quarter-chord axis of the rotor blade at a distance of 0.4 chords. The vortex core radius for the calculation was set equal to the experimentally estimated value of 0.15 chords. Predicted pressure results showed little sensitivity to vortex core size.

The blade-vortex interaction calculations were started with a quasi-steady solution at $\psi = 30^\circ$. Each time-step covered 0.25° of rotor azimuthal angle until the rotor reached $\psi = 175^\circ$. At this point, the rotor is close to the vortex and the time-step was cut to 0.1° . Computer time for the calculation is approximately 0.83 seconds per time-step on a CRAY XMP-12 computer system. Total CPU time for these calculations was approximately 10 minutes.

There is some question as to the accuracy of the vortex strengths reported for this experiment. Srinivasan et al. [17] have compiled a large amount of experimental data for vortex velocity distributions from NACA 0015 wings. Based on this data, their calculation used a nondimensional vortex strength $\Gamma_v = 0.133$, which was approximately 80% of the value reported by Caradonna et al. [16]. The calculations in this paper use the vortex strengths that were determined by Srinivasan et al. [17].

Figure 8 shows the results from this calculation. Pressure coefficients are presented at the $r/R = 0.893$ spanwise station for a series of rotor azimuthal angles. The predictions show excellent agreement with the experimental data, especially in the crossover region from negative-to-positive lift. The main discrepancy between the prediction and the data is the presence of a slight pressure wave in the predicted lower surface pressure. This pressure wave is located directly above the vortex as the rotor passes over it. It does not appear to be present in the experimental data and may be the result of neglecting the temporal derivative terms in Eq. (12).

Computations have also been performed for a supercritical case, $M_T = 0.8$. The data in this case involves interactions where the shock persists up to and throughout the interaction. To date, all computational attempts at this case have been unsuccessful because the computed shock collapses prematurely in the second quadrant (by approximately 5°). The reasons for this are not yet known.

To demonstrate that the FPR code can qualitatively predict a transonic blade-vortex interaction if the shock persists, the tip Mach number for the computer simulation was raised to $M_T = 0.82$. The results are shown in Fig. 9. The higher tip Mach number ensured that the shock structure was in better agreement with the data at the start of the blade-vortex encounter ($\psi = 170^\circ$). With this adjustment, it is clear that the computer prediction demonstrates the major features of the transonic blade-vortex interaction. The shock on the upper surface disappears rapidly, while the lower surface shock moves forward more slowly toward the leading edge of the rotor. The unsteady shock motion on the vortex side of the rotor is the dominant feature in the flow. It could have major effects on rotor acoustics and on the blade higher harmonic loading.

8. CONCLUSIONS

1. The FPR code has been coupled to the CAMRAD wake model. The result is a hybrid integral-differential rotor flow scheme. Successful prediction of two advancing rotor cases has been demonstrated.
2. A "split-potential" formulation has been developed for computing three-dimensional, unsteady blade-vortex interactions. Discrete vortices are implicitly coupled to a conservative full-potential model for the rotor aerodynamics.
3. The split-potential FPR code has been used to obtain good results for a subcritical blade-vortex interaction case. Qualitatively realistic results have been shown for a blade-vortex interaction in a supercritical case. Results thus far have been limited to simplified geometries and a single vortex. More complex blade-vortex interactions will be studied in future work.

9. REFERENCES

1. Johnson, W., "A Comprehensive Analytical Model of Rotorcraft Aerodynamics and Dynamics. Part 1, Analysis Development," NASA TM-81182, 1980.
2. Caradonna, F. X., Tung, C., and Desopper, A., "Finite-Difference Modeling of Rotor Flows Including Wake Effects," *J. Am. Hel. Soc.*, Vol. 29, April 1984, pp. 26-33.

3. Tung, C., Caradonna, F. X., Boxwell, D. A., and Johnson, W. R., "The Prediction of Transonic Flows on Advancing Rotors," AHS 40th Annual Forum, May, 1984.
4. Tung, C., and Chang, I. C., "Rotor Transonic Computation with Wake Effect," *Fourth International Conference on Applied Numerical Modeling*, Taiwan, China, 27-29 Dec., 1984.
5. Caradonna, F. X., and Tung, C., "Finite-Difference Computations of Rotor Loads," Presented at the American Helicopter Society, Nanjing Aeronautical Institute Conference, Nanjing, China, Nov. 6-8, 1985.
6. Chang, I-Chung, and Tung, C., "Numerical Solution of the Full-Potential Equation for Rotors and Oblique Wings using a New Wake Model," AIAA Paper 85-0268, Jan. 1985.
7. Strawn, R. C., and Caradonna, F. X., "Numerical Modeling of Rotor Flows with a Conservative Form of the Full-Potential Equations," AIAA Paper 86-0079, Jan. 1986.
8. Bridgeman, J. O., Steger, J. L., and Caradonna, F. X., "A Conservative Finite-Difference Algorithm for the Unsteady Transonic Potential Equation in Generalized Coordinates," AIAA Paper 82-1388, Aug. 1982.
9. Chang, I-Chung, "Transonic Flow Analysis for Rotors, Part 2 Three-Dimensional, Unsteady, Full-Potential Calculation," NASA Technical Paper 2375, Jan. 1985.
10. Boxwell, D. A., Schmitz, F. H., Spletstoesser, W. R., and Schultz, K. J., "Model Helicopter Rotor High-Speed Impulsive Noise: Measured Acoustics and Blade Pressures," NASA TM-85850, 1983.
11. Philippe, J. J., and Chattot, J. J., "Experimental and Theoretical Studies on Helicopter Blade Tips at ONERA," Presented at the Sixth European Rotorcraft and Powered Lift Aircraft Forum, Bristol, U.K., Paper No. 46, Sept., 1980, pp 16-19.
12. Jones, H., "Full-Potential Modeling of Blade-Vortex Interactions," Ph. D. thesis, George Washington University, to be published in July, 1986.
13. Sankar, N. L., and Malone, J. B., "Unsteady Transonic Full-Potential Solutions for Airfoils Encountering Vortices and Gusts," AIAA Paper 85-1710, July, 1985.
14. McCroskey, W. J., "The Effects of Gusts on the Fluctuating Airloads of Airfoils in Transonic Flow," AIAA Paper 84-1580, June, 1984.
15. Sankar, N. L. and Tang, W., "Numerical Solution of Unsteady Viscous Flow Past Rotor Sections," AIAA Paper 85-0129.
16. Caradonna, F. X., Laub, G. H., and Tung, C., "An Experimental Investigation of the Parallel Blade-Vortex Interaction," Presented at the 10th European Rotorcraft Forum, Aug. 28-31, 1984, The Hague, Netherlands.
17. Srinivasan, G. R., McCroskey, W. J., and Baeder, J. D., "Aerodynamics of a Two-Dimensional Blade-Vortex Interaction," AIAA Paper 85-1560, July, 1985.

9. ACKNOWLEDGEMENTS

The authors would like to thank Dr. Frank Caradonna of the Army Aeroflightdynamics Directorate for his technical advice and support for this work. We would also like to thank Mr. Henry Jones, also of the Army Aeroflightdynamics Directorate, for his useful discussion of the blade-vortex interaction model.

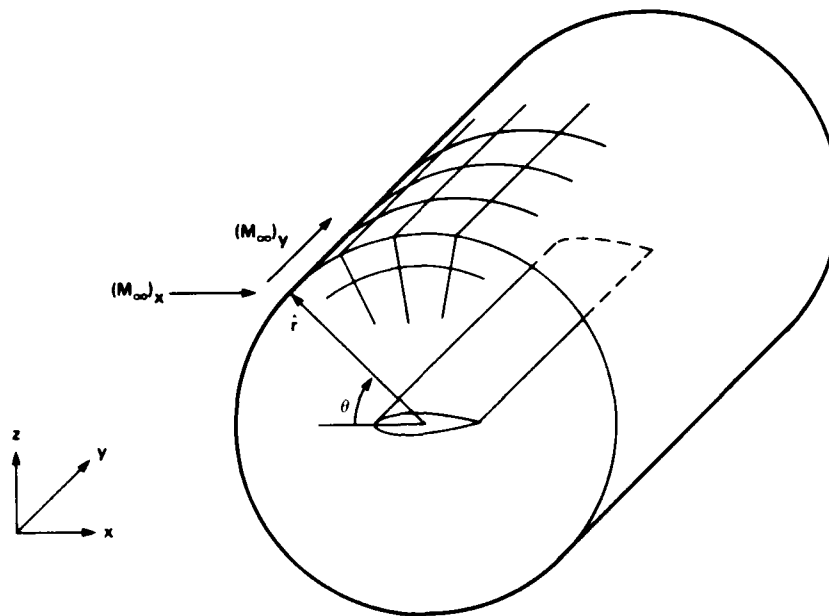


Fig. 1 Coordinate system for a nonreflection boundary condition.

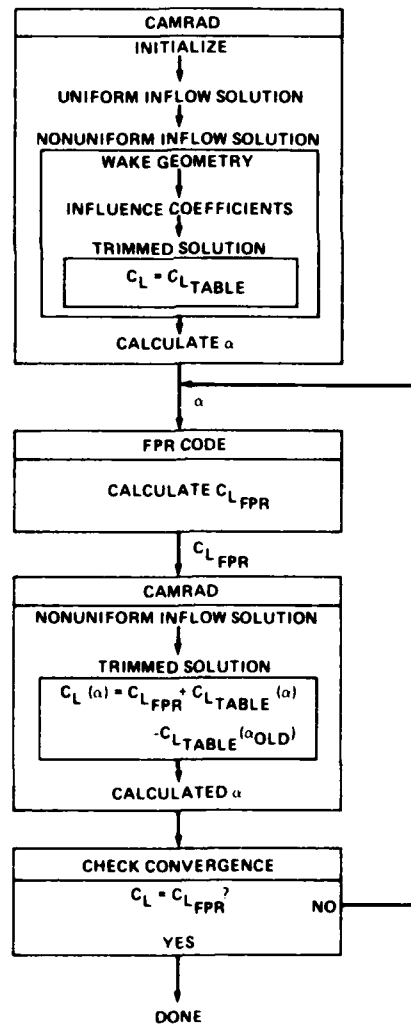


Fig. 2 A hybrid integral-differential rotor flow scheme.

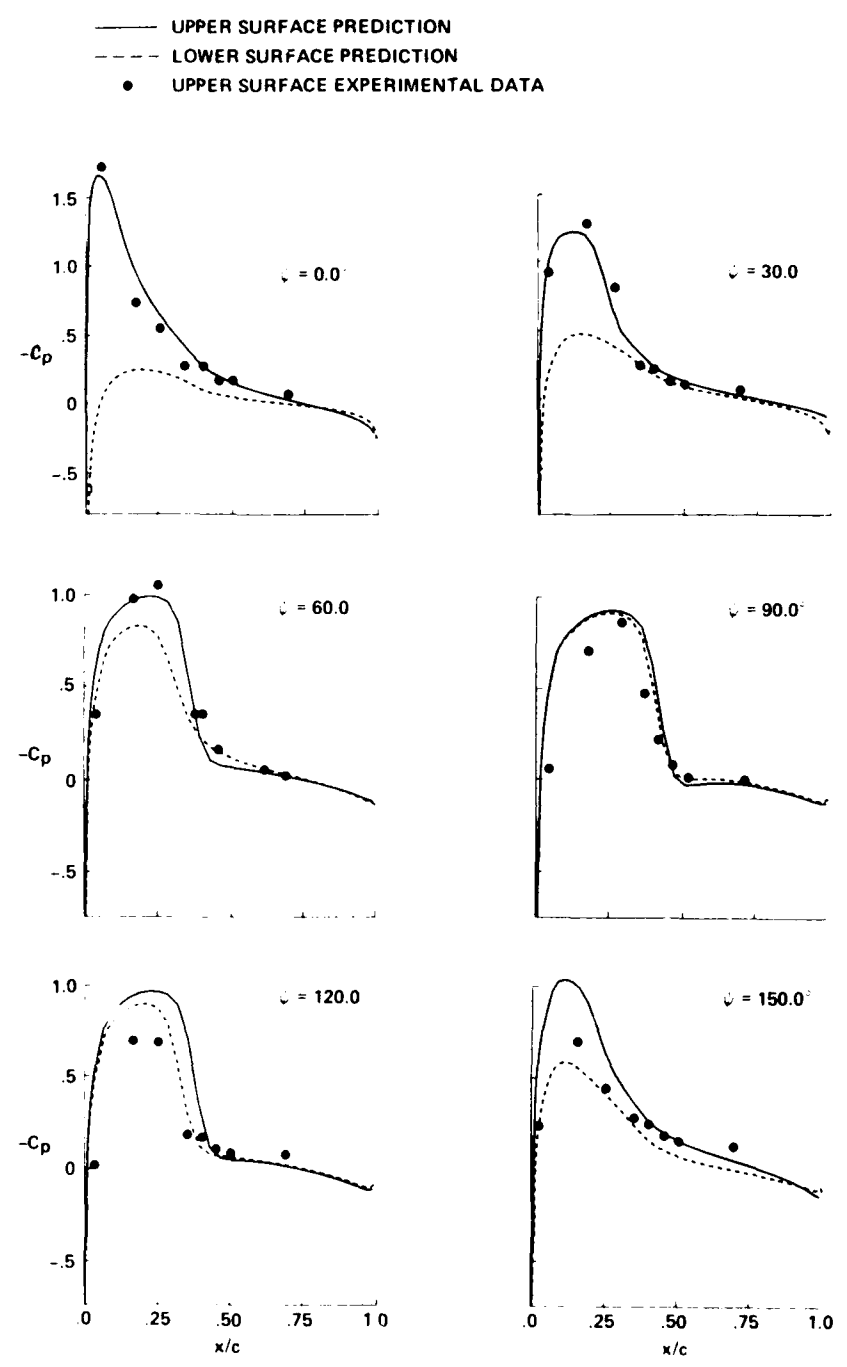


Fig. 3 Surface pressure results for the two-bladed OLS advancing rotor. $M_T = 0.663$, $\mu = 0.298$, $AR = 13.7$, $r/R = 0.95$, $C_T \sigma = 0.0769$.

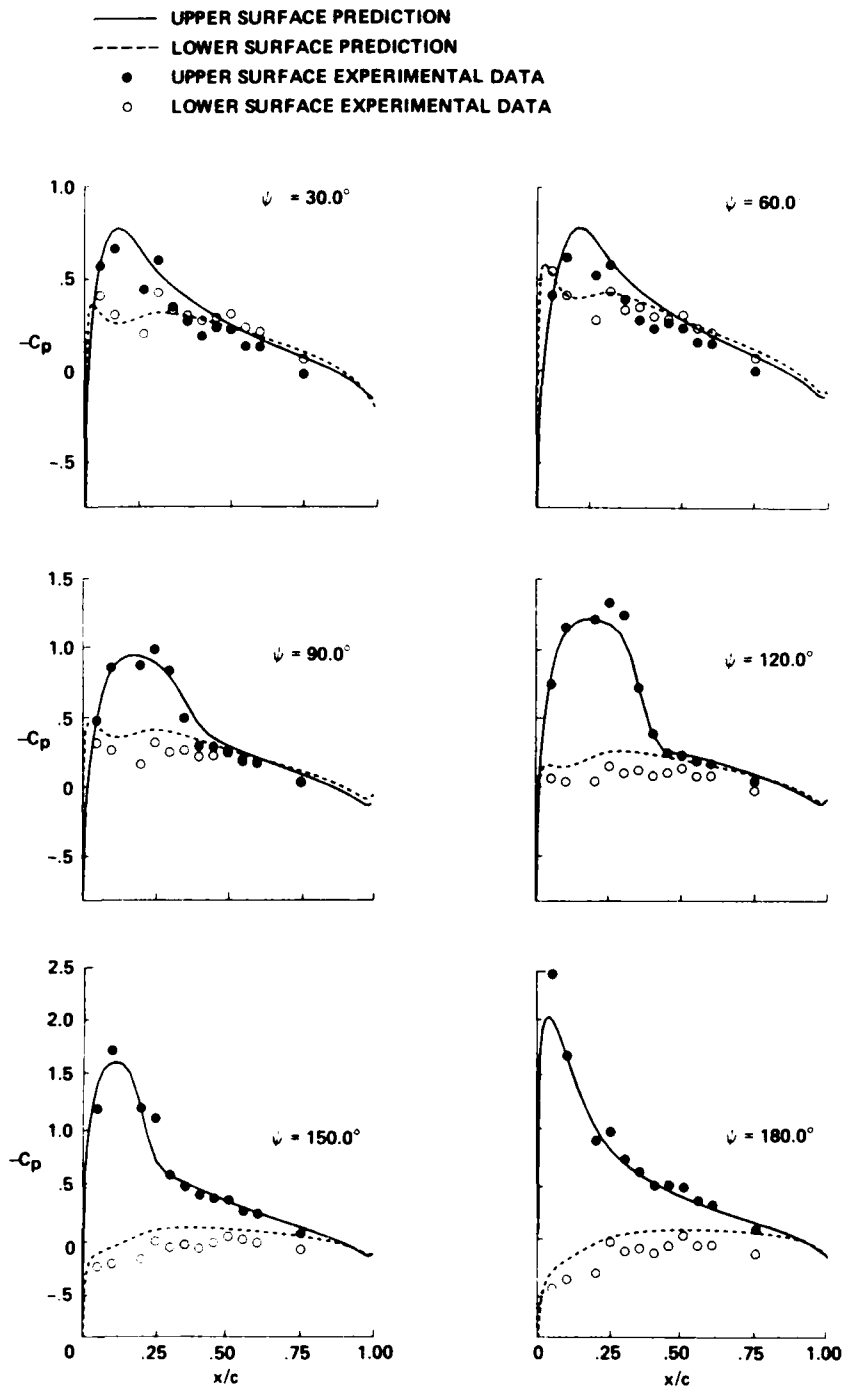


Fig. 4 Surface pressure results for the ONERA three-bladed rotor. $M_T = 0.629$, $\mu = 0.387$, $AR = 6.968$, $r/R = 0.85$, $C_T \sigma = 0.0665$.

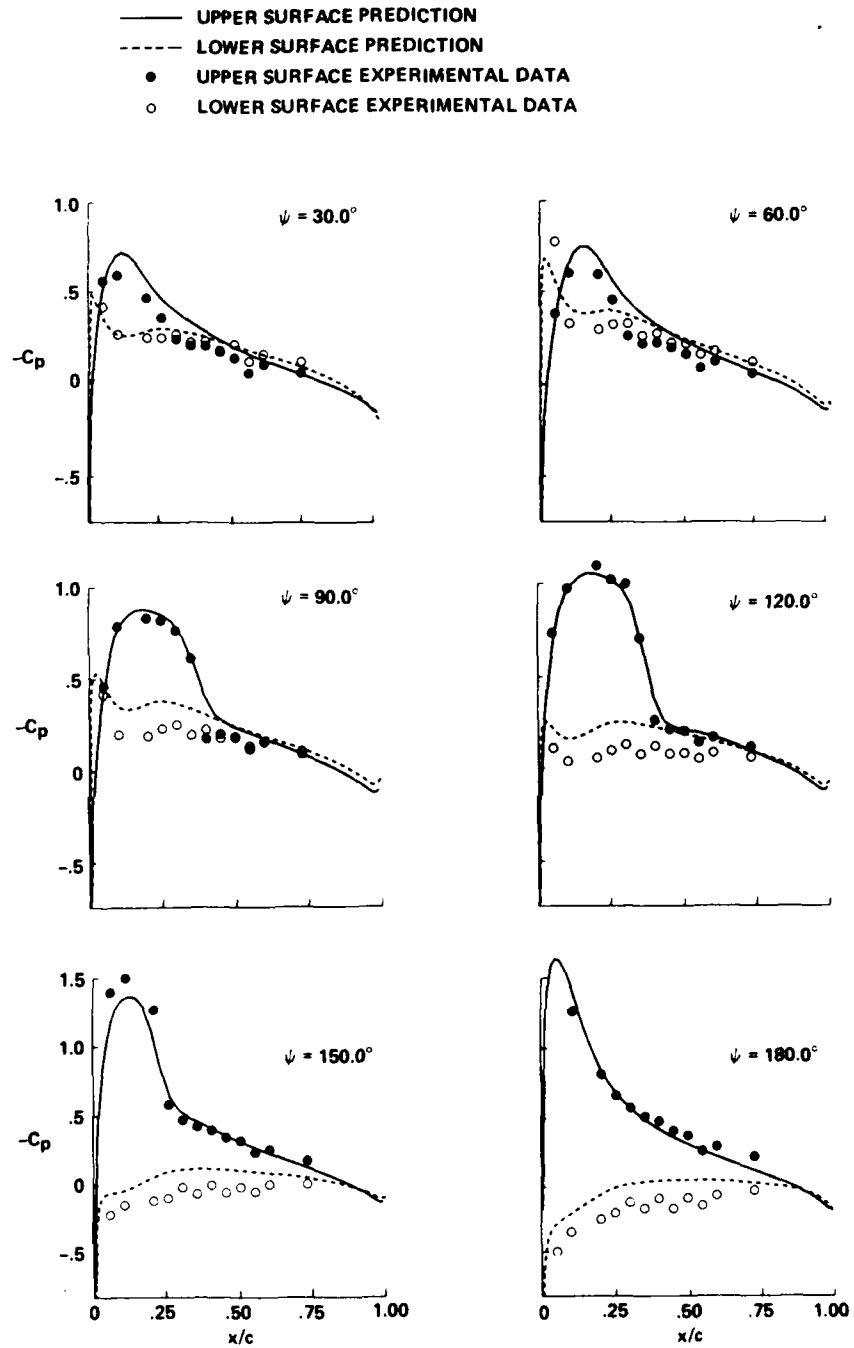


Fig. 5 Surface pressure results for the ONERA three-bladed rotor. $M_i = 0.629$, $\mu = 0.387$, $AR = 6.968$, $r/R = 0.90$, $C_T/\sigma = 0.0665$.

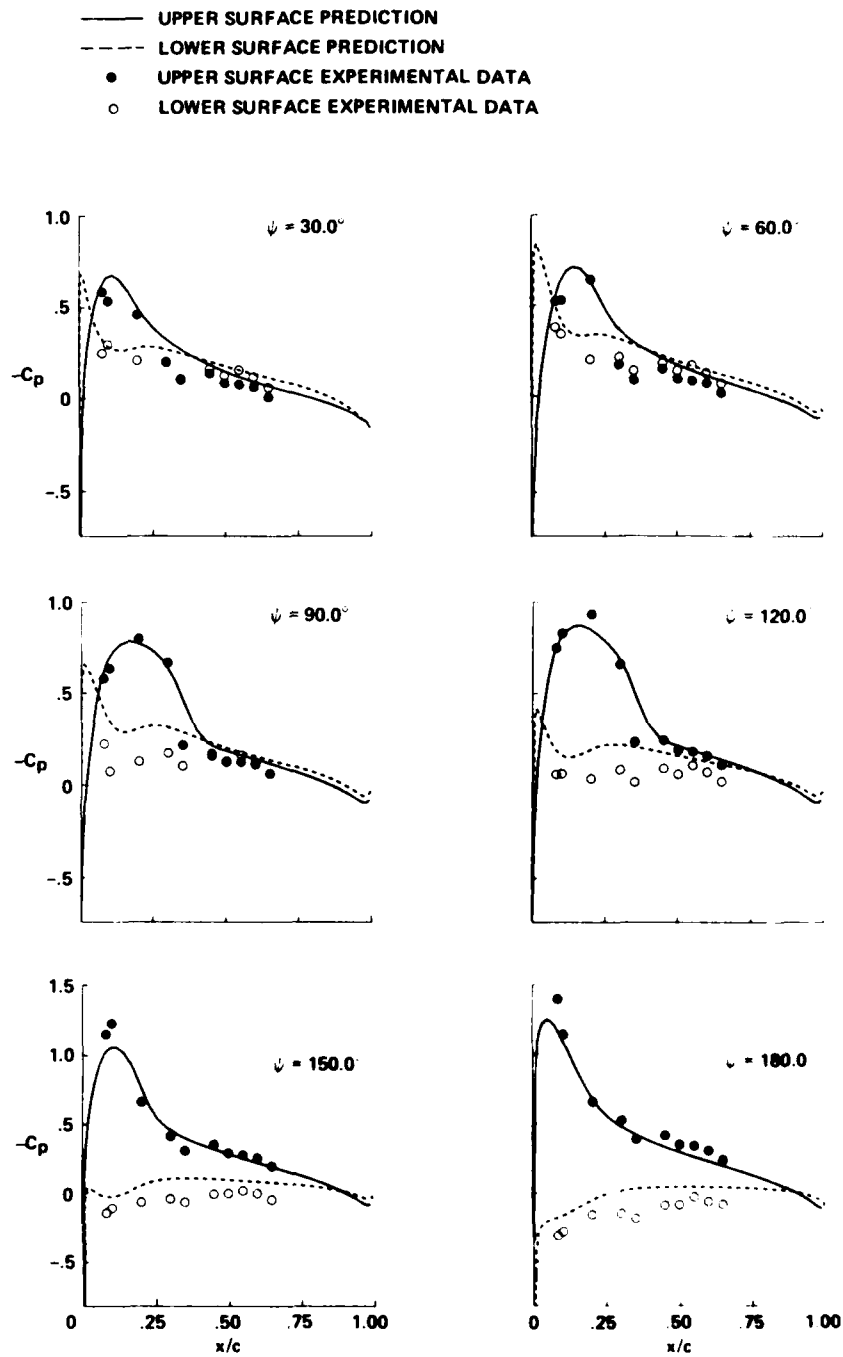


Fig. 6 Surface pressure results for the ONERA three-bladed rotor. $M_T = 0.629$, $\mu = 0.387$, $AR = 6.968$, $r/R = 0.95$,
 $C_T/\sigma = 0.0665$.

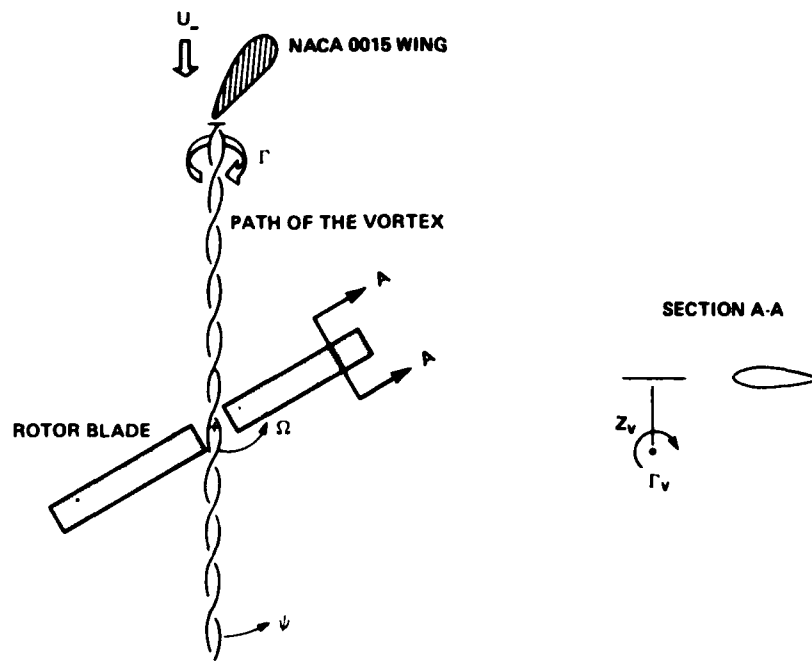


Fig. 7 Rotor-vortex interaction experiment in Ref. 16.

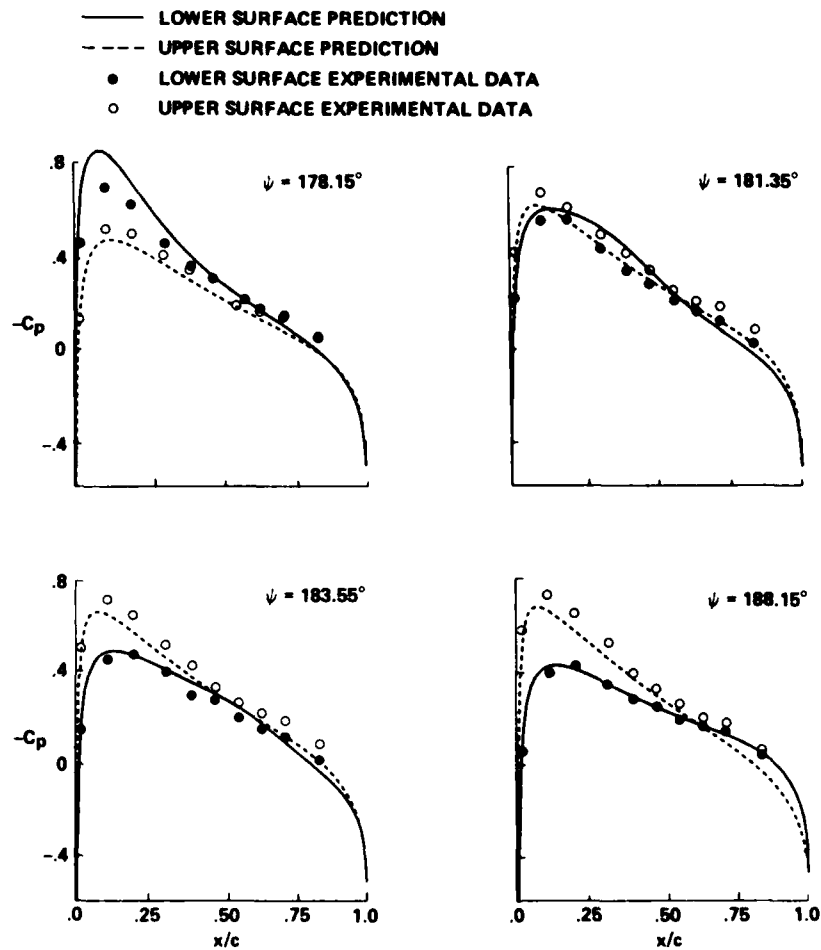


Fig. 8 Surface pressure results for a three-dimensional blade-vortex interaction, $\Gamma_v = 0.133$, $Z_v/c = 0.4$, $M_T = 0.6$, $\mu = 0.2$, $AR = 7.0$, $r/R = 0.893$, $\alpha = 0$, untwisted, untapered, NACA 0012 blade.

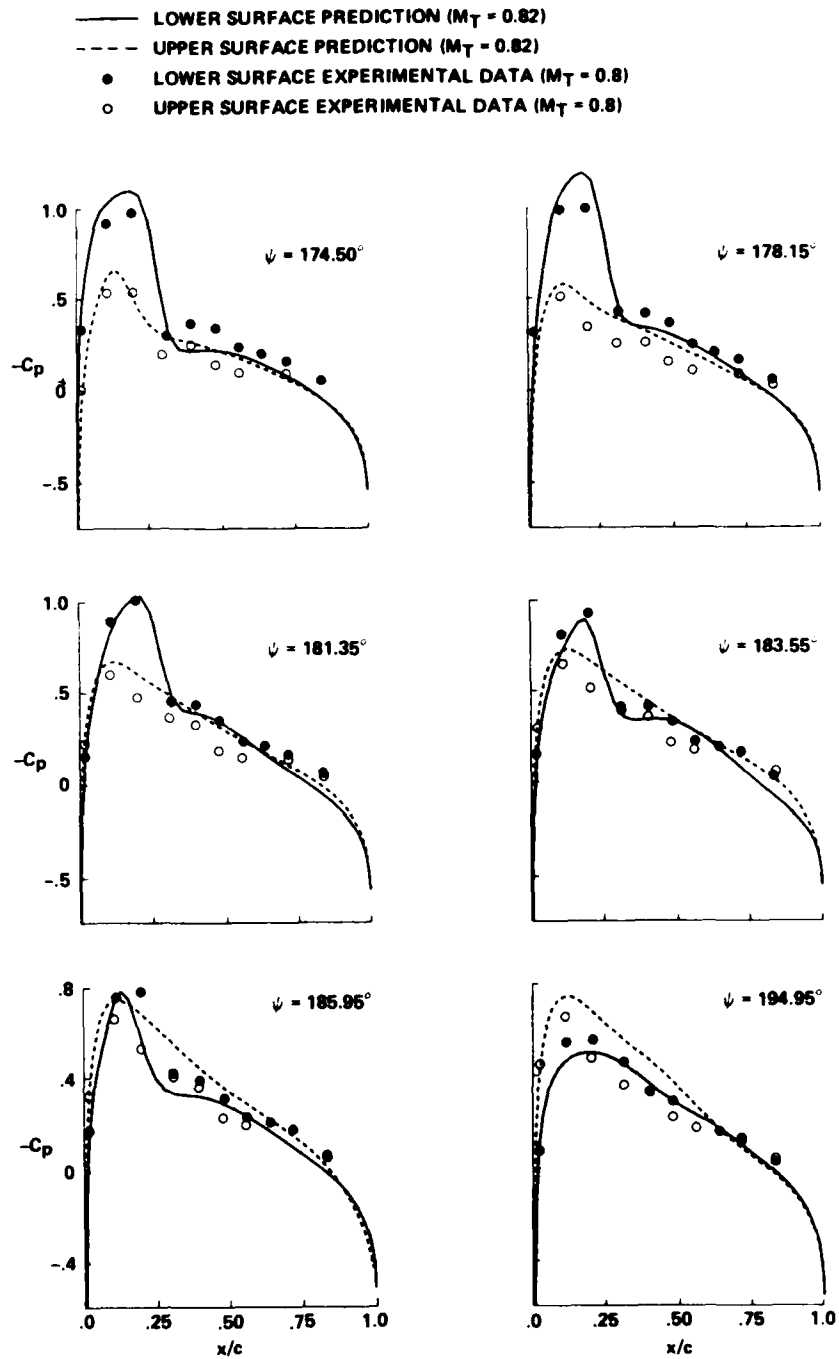


Fig. 9 Surface pressure results for a three-dimensional blade-vortex interaction, $\Gamma_v = 0.177$, $Z_v/c = 0.4$, $\mu = 0.2$, $AR = 7.0$,
 $r/R = 0.893$, $\alpha = 0$, untwisted, untapered, NACA 0012 blade. Data has $M_T = 0.8$, prediction is for $M_T = 0.82$.

1 Report No. NASA TM-88238 USAVSCOM TM-86-A-1		2 Government Accession No. AD-A168217		3 Recipient's Catalog No.	
4 Title and Subtitle THE PREDICTION OF TRANSONIC LOADING ON ADVANCING HELICOPTER ROTORS				5 Report Date April 1986	
				6 Performing Organization Code A-86198	
7 Author(s) R. C. Strawn and C. Tung				8 Performing Organization Report No.	
				10 Work Unit No.	
9 Performing Organization Name and Address Ames Research Center and Aeroflightdynamics Directorate, U.S. Army Aviation and Technology Activity-AVSCOM, Ames Research Center, Moffett Field, CA 94035				11 Contract or Grant No.	
				13 Type of Report and Period Covered Technical Memorandum	
12 Sponsoring Agency Name and Address National Aeronautics and Space Administration Washington, DC 20546, and U. S. Army Aviation Systems Command, St. Louis, MO 63120				14 Sponsoring Agency Code	
				15 Supplementary Notes Point of Contact: Roger Strawn, Ames Research Center, MS 215-1, Moffett Field, CA 94035 (415) 694-5902 or FTS 464-5902	
16 Abstract -Two different schemes are presented for including the effect of rotor wakes on the finite-difference prediction of rotor loads. The first formulation includes wake effects by means of a blade-surface inflow specification. This approach is sufficiently simple to permit coupling of a full-potential finite-difference rotor code to a comprehensive integral model for the rotor wake and blade motion. The coupling involves a transfer of appropriate loads and inflow data between the two computer codes. Results are compared with experimental data for two advancing rotor cases. The second rotor wake modeling scheme in this paper is a "split potential" formulation for computing unsteady blade-vortex interactions. Discrete vortex fields are introduced into a three-dimensional, conservative, full-potential rotor code. Computer predictions are compared with two experimental blade-vortex interaction cases.					
17 Key Words (Suggested by Author(s)) Rotor, Full-potential equation Transonic Blade-vortex interaction Wake modeling			18 Distribution Statement Unlimited Subject category - 02		
19 Security Classif. (of this report) Unclassified		20 Security Classif. (of this page) Unclassified		21 No. of Pages 17	22 Price*

END

DATE

7-86